REPORT DOCUMENTATION PAGE

Form Approved
OMB No. 074-0188

1. AGENCY USE ONLY (Leave blank)	2. REPORT DATE	3. REPORT TYPE AND DATES COVERED
	March 31, 2009	

4. TITLE AND SUBTITLE

Low-Temperature Superplasticity of Ultra-Fine-Grained Ti-6Al-2Sn-4Zr-2Mo-0.1Si Alloy

5. FUNDING NUMBERS

FA4869-08-1-4001

6. AUTHOR(S)

Chan Hee Park and Chong Soo Lee

7. PERFORMING ORGANIZATION NAME(S) AND ADDRESS(ES)

Pohang University of Science and Technology

San 31, Hyoja-dong, Pohang 790-784, KOREA

8. PERFORMING ORGANIZATION REPORT NUMBER

9. SPONSORING / MONITORING AGENCY NAME(S) AND ADDRESS(ES)

Asian Office of Aerospace Research and Development
7-23-17 Roppongi, Minato-ku, Tokyo 106-0032
(Tel) 81-3-5410-4409 (Fax) 81-3-5410-4407

10. SPONSORING / MONITORING AGENCY REPORT NUMBER

11. SUPPLEMENTARY NOTES

12a. DISTRIBUTION / AVAILABILITY STATEMENT

12b. DISTRIBUTION CODE

13. ABSTRACT

This study aimed to achieve low-temperature superplasticity of Ti-6Al-2Sn-4Zr-2Mo-0.1Si alloy utilizing dynamic globularization, and to elucidate the deformation mechanisms in the context of inelastic-deformation theory. The as-received microstructure with equiaxed-alpha grain/particle size of 13 μm was refined to 2.2 μm by dynamic globularization at 775 °C, which was confirmed by electron back-scattered diffraction (EBSD) analysis. Uniaxial tension tests were carried out for both coarse (starting material) and fine (dynamically globularized materials) grained materials at strain rate range of 10^{-4} ~ 10^{-2} s^{-1} and temperature range of 650 to 750 °C. The total elongation of fine grained microstructure (382-826 %) was considerably enhanced as compared to that of coarse grained microstructure (189-286 %) at 10^{-4} s^{-1}. With respect to the microstructural evolution, the dynamic coarsening rate of alpha phase during deformation was ~12 times faster than that of static coarsening, and both static and dynamic coarsening rate for Ti-6Al-2Sn-4Zr-2Mo-0.1Si alloy were ~2 to 4 times lower than those for Ti-6Al-4V alloy, which was attributed to lower diffusivity of rate-limiting solute at the similar test temperature. It was found that the mechanism of the low-temperature superplasticity of Ti-6Al-2Sn-4Zr-2Mo-0.1Si alloy was grain boundary sliding (GBS) accommodated by dislocation motion with both stress exponent (n) and grain size exponent (p) values of ~2. When the alpha grain/particle size was considered to be an effective grain size, the apparent activation energy for low temperature superplasticity of Ti-6Al-2Sn-4Zr-2Mo-0.1Si alloy (~169 kJ/mol) was close to that of Ti-6Al-4V alloy (~160 kJ/mol). Finally, internal-variable theory manifested that the enhanced superplasticity in dynamically globularized microstructure was attributed to lager GBS fraction and lower friction stress than coarse grained microstructure.

14. SUBJECT TERMS	15. NUMBER OF PAGES
	41
	16. PRICE CODE

17. SECURITY CLASSIFICATION OF REPORT	18. SECURITY CLASSIFICATION OF THIS PAGE	19. SECURITY CLASSIFICATION OF ABSTRACT	20. LIMITATION OF ABSTRACT

A Research Report to AFOSR/AOARD
(Project Number: FA4869-08-1-4001)

Low-Temperature Superplasticity of Ultra-Fine-Grained Ti-6Al-2Sn-4Zr-2Mo-0.1Si Alloy

by

Chan Hee Park and Chong Soo Lee
Department of Materials Science and Engineering
Pohang University of Science and Technology
Pohang 790-784, KOREA

March 31, 2009

ABSTRACT

This study aimed to achieve low-temperature superplasticity of Ti-6Al-2Sn-4Zr-2Mo-0.1Si alloy utilizing dynamic globularization, and to elucidate the deformation mechanisms in the context of inelastic-deformation theory. The as-received microstructure with equiaxed-alpha grain/particle size of 13 μm was refined to 2.2 μm by dynamic globularization at 775 °C, which was confirmed by electron back-scattered diffraction (EBSD) analysis. Uniaxial tension tests were carried out for both coarse (starting material) and fine (dynamically globularized materials) grained materials at strain rate range of 10^{-4} ~ 10^{-2} s^{-1} and temperature range of 650 to 750 °C. The total elongation of fine grained microstructure (382-826 %) was considerably enhanced as compared to that of coarse grained microstructure (189-286 %) at 10^{-4} s^{-1}. With respect to the microstructural evolution, the dynamic coarsening rate of alpha phase during deformation was ~12 times faster than that of static coarsening, and both static and dynamic coarsening rate for Ti-6Al-2Sn-4Zr-2Mo-0.1Si alloy were ~2 to 4 times lower than those for Ti-6Al-4V alloy, which was attributed to lower diffusivity of rate-limiting solute at the similar test temperature. It was found that the mechanism of the low-temperature superplasticity of Ti-6Al-2Sn-4Zr-2Mo-0.1Si alloy was grain boundary sliding (GBS) accommodated by dislocation motion with both stress exponent (n) and grain size exponent (p) values of ~2. When the alpha grain/particle size was considered to be an effective grain size, the apparent activation energy for low temperature superplasticity of Ti-6Al-2Sn-4Zr-2Mo-0.1Si alloy (~169 kJ/mol) was close to that of Ti-6Al-4V alloy (~160 kJ/mol). Finally, internal-variable theory manifested that the enhanced superplasticity in dynamically globularized microstructure was attributed to lager GBS fraction and lower friction stress than the coarse grained microstructure.

Contents

1. Introduction ----------5

2. Internal-variable theory----------7

2.1. Dislocation kinematics----------7

2.2. Observable deformation variables----------12

2.3. Constitutive relations----------13

2.4. Constitutive relationship for superplasticity----------16

3. Materials and experimental procedures----------20

4. Results----------23

4.1. Flow behavior and elongation to failure----------23

4.2. Load-relaxation behavior----------25

5. Discussion----------28

5.1. Dynamic and static coarsening kinetics----------28

5.2. Deformation mechanism of dynamically globularized Ti6242S alloy----------32

5.3. Quantitative analysis on deformation mechanisms of CG and UFG materials------37

6. Summary----------39

References----------40

1. Introduction

The alpha/beta titanium alloys are widely used for aerospace application due to its high specific strength, excellent corrosion resistance, and reasonable high-temperature strength [1]. Especially, Ti-6Al-2Sn-4Zr-2Mo-0.1Si alloy has been used as turbine engine blade and compressor disc due to superior creep resistance and higher practical temperature (~550 ^{o}C) as compared to conventional Ti-6Al-4V alloy (~350 ^{o}C) [1,2]. In particular, high formability of this alloy associated with superplastic forming (SPF) provides weight reduction as well as cost savings. However, in spite of these commercial benefits, its wide industrial application was restricted by uneconomical processing conditions such as high temperature (≥900 ^{o}C) and/or low strain rate (≤10^{-3} s^{-1}) [3,4]. Accordingly, extensive investigations were conducted on the low-temperature (≤750 ^{o}C) and/or high-strain rate (≥10^{-2} s^{-1}) superplasticity by use of grain refinement through severe plastic deformation (SPD), *i.e.*, high pressure torsion (HPT), equal channel angular pressing (ECAP) and accumulated roll bonding (ARB) [5-8]. Also, recently, enhanced superplasticity of Ti-6Al-4V alloy utilizing dynamic globularization, *i.e.*, the conversion of the transformed beta microstructure to a fine equiaxed microstructure, was reported [9]. All these efforts make it possible to achieve faster production cycle and cheaper die cost.

Many efforts were also made to elucidate the deformation mechanism associated with microstructural evolution during superplastic deformation. For instant, Mukherjee, Bird, and Dorn [10] established single-mechanism model for various materials, while Gifkins [11] and Bae and Ghosh [12] developed two-mechanism theory describing mantle/core deformation. Recently, Ko *et al*. [13] quantitatively investigated low-temperature deformation mechanisms of Ti-6Al-4V alloy with submicrocrystalline microstructure in the context of internal-variable theory. Also, the static and dynamic coarsening behaviors of ultrafine-grained (UFG) Ti-6Al-4V alloy were interpreted in terms

of modified LSW theory by Semiatin *et al*. [14,15]. More recently, Sargent *et al*. [16] emphasized that the importance of alpha-particle size having high angle boundaries to describe the superplastic flow of ultrafine Ti-6Al-4V alloy rather than alpha sub-grain or beta grain size.

Although the previous research works on microstructural evolution and plastic flow behavior of alpha/beta titanium alloy reported enhanced superplasticity and provided insight into overall deformation mechanisms, most of efforts were focused on Ti-6Al-4V alloy, not on the Ti-6Al-2Sn-4Zr-2Mo-0.1Si alloy. Here, it is of great interest to investigate the role of rate-limiting solutes such as Mo and V on microstructural evolution of alpha/beta titanium alloys during superplasticity. Despite its practical importance, the possibility of low-temperature superplasticity for Ti-6Al-2Sn-4Zr-2Mo-0.1Si alloy utilizing dynamic globularization has not identified yet. Another aspect is related with the activation energy for superplastic deformation of alpha/beta titanium alloy (160-330 kJ/mol), which is still in the controversy [13, 16-20]. Therefore, the purposes of the present study are to achieve enhanced superplasticity of Ti-6Al-2Sn-4Zr-2Mo-0.1Si alloy utilizing dynamic globularization and to investigate the effect of rate-limiting solute, Mo, on microstructural evolution (in terms of static and dynamic grain growth) and deformation mechanism, whose diffusivity is noticeably slower than V in Ti-6Al-4V alloy. In addition, quantitative analysis on the contribution of the grain-matrix deformation (GMD) and grain-boundary sliding (GBS) to overall deformation was made in the context of internal-variable theory.

2. Internal-variable theory

The superplastic deformation behavior of crystalline materials has been described phenomenologically by a power law relationship between the two external variable, *viz.* flow stress (σ) and strain rate ($\dot{\varepsilon}$), with a power index *m*. The value of *m* is defined as the slope of log σ *vs* log $\dot{\varepsilon}$ curves and generally called the strain rate sensitivity parameter. This parameter has widely been used as a representative variable to characterize superplastic deformation behavior [21,22]. In general, it is believed that a large value of *m* is required for superplastic deformation, observed to vary continuously on log σ *vs* log $\dot{\varepsilon}$ curve and furthermore there is no critical value of m, above which superplastic deformation can be predicted. It is believed, in this regard, that the phenomenological power law relationship may not be a suitable constitutive relationship for superplastic deformation. Therefore, it is attempted to formulate a new physically based superplasticity theory utilizing the concept of internal state variables [23] instead of the conventionally used external variables.

2.1. Dislocation kinematics

An elementary material volume V bounded by a surface S "within" and "across" which dislocations are allowed to move in response to an applied stress as in Fig. 1 is considered. When the material boundary acts as a "barrier" partially blocking the passage of dislocation, some of them would remain inside the material volume giving rise to an internal strain. While at the same time the rest will pass through to produce an externally observable material deformation. These simultaneous processes of accumulation within V and the passage through S of dislocations are believed to be the most fundamental deformation mechanism responsible for various mechanical-phenomena.

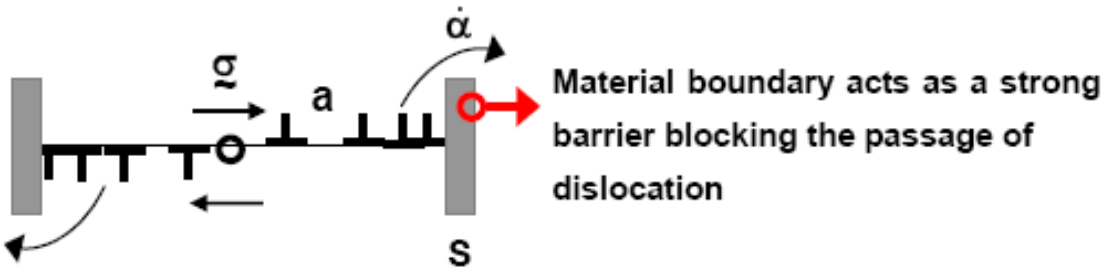

Figure 1. An internal variable model for inelastic deformation.

To examine the internal deformation, the total inelastic deformation excluding the usual elastic part together with a possibly concurring rigid body rotation is conveniently assumed to occur in two successive steps as schematically depicted in Fig. 2. The material volume is first regarded as fixed in the "external observer frame" (χ) to isolate the internal motion of dislocation. By assigning a "material reference frame" (ζ) attached to the material volume, the motion of dislocation is specified by a displacement vector λ from which the dislocation velocity v can be defined as its material time rate. The two unit vectors s and m in Fig. 2 are attached to the dislocation and thus represent the "internal observer frame" together with the unit line sense vector t, tangent to the dislocation line. It is also noted that a general rotation of the dislocations is allowed in this process. Our attention here is focused on this internal deformation process occurring in the material volume V fixed in space as depicted in Fig. 2.

Following the usual continuum approach for dislocation, the density distribution function $\rho(\zeta,t)$ is prescribed in reference to the material frame by including the production/annihilation rate term $\dot{c}$.

$$\frac{\partial \rho}{\partial \rho} = \nabla_{\zeta} \cdot (\rho v) = \rho \dot{c} \tag{1}$$

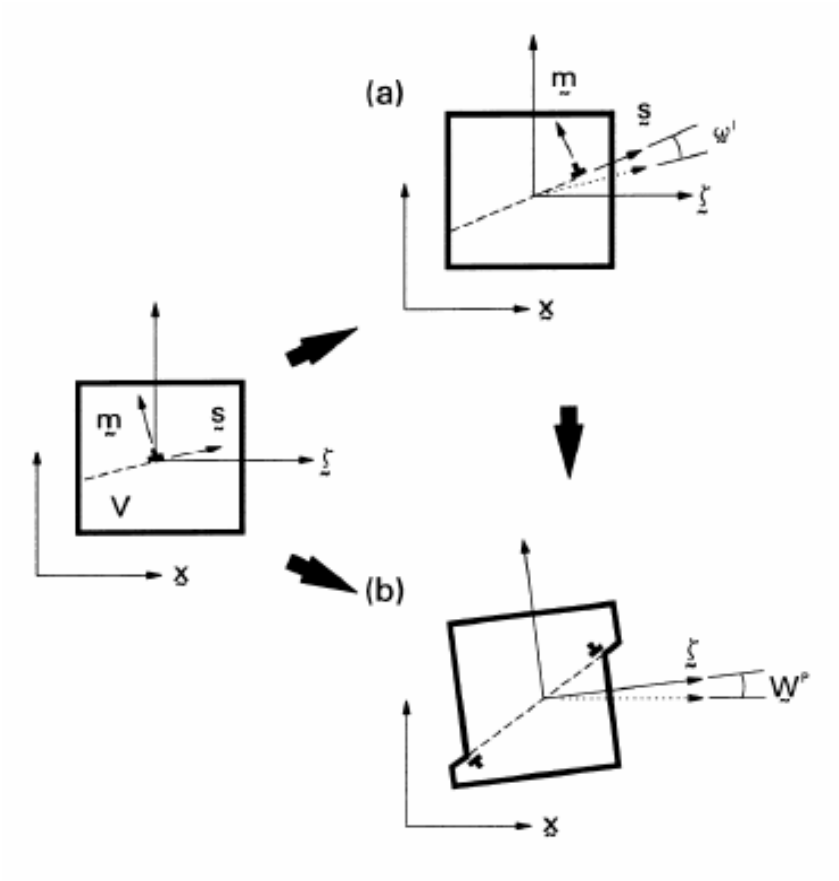

Figure 2. Dislocation motion in two successive stages: (a) internal motion produces internal distortion (β) and spin (ϖ^I); (b) dislocation flux across the material boundary generates non-recoverable deformation and plastic spin (W^p). [23]

The elementary material volume V is further taken in such a way that all of the dislocations within V have the same Burgers vector b and glide direction s. Since dislocation glide is a conservative motion producing material distortion, a symmetric internal distortion tensor can be defined by

$$\beta(\zeta, t) = b\rho\lambda M \tag{2}$$

$$M = \frac{1}{2}(sm + ms) \tag{3}$$

Here b denotes the magnitude of the burgers vector b, λ the glide distance parameter (λ=λ s) and M the glide orientation tensor. In this way, the variable has the unit of strain and represents the symmetric part of the internal distortion intensity at each material point with the unique reference state of β=0 when no glide dislocations accumulate inside V. The time rate of change of β in reference to the material frame held fixed with respect to the external observer is now sought. Differentiating Eq. (2) with respect to time holding ζ fixed and using Eq. (1), the following is obtained after rearrangement,

$$\frac{\partial \beta}{\partial t} = \dot{c}\beta - \nabla_{\zeta} \cdot \beta v + b\rho\lambda\partial M + b\rho\lambda \frac{\partial M}{\partial t} + \left(\lambda \cdot \frac{\partial s}{\partial t}\right) M \tag{4}$$

where ν denotes the glide velocity (ν = v s) and spatially independent condition of s = m = 0 in V were also used. Eq. (4) is written in reference to the material frame and in order to express it with respect to the internal observer frame, the internal rotation of dislocations should be considered. To this end it is noted that an accumulation of glide dislocations within a material volume V not only produces internal distortion but also internal rotation. An internal spin tensor ϖ^{I} can then be identified in association with the rotation of slip zones in a fixed material volume. The internal rotation, together with the internal distortion, is believed to be accommodated by the elastic surroundings to compensate the incompatibility due to the accumulation of dislocation. It is emphasized again that here the exclusive concerns are the deformation and rotation process due only to dislocations from an internal observer's point of view. In this way, standard local elastic deformations and rigid body rotations are explicitly excluded.

Next, rate with respect to an internal observer who, by definition, sees no time rate of change of the orientation quantities s, m and M are considered. In view of the spatial independence assumption for these quantities the co-rotational rates of the vector s and the second order tensor M and β, seen by an internal observer, can then be written as

$$\dot{s} = \frac{\partial s}{\partial t} - \varpi^I \cdot s \tag{5}$$

$$\dot{M} = \frac{\partial M}{\partial t} - \varpi^I \cdot M + M \cdot \varpi^I \tag{6}$$

$$\dot{\beta} = \frac{\partial \beta}{\partial t} - \varpi^I \cdot \beta + \beta \cdot \varpi \tag{7}$$

Utilizing these together with the fact that $\dot{s} = \dot{M} = 0$, Eq. (4) can now be reduced into the simpler form of

$$\dot{\beta} + \nabla_\zeta \cdot (v\beta) = \left(\dot{c} + \frac{\nu}{\lambda} \right) \beta \tag{8}$$

It is remarked that Eq. (8) is the evolution equation of β expressed in reference to the material frame and has the form of a complete balance law for tensor variables containing both a flux term and a rate term taken co-rotationally with an “internal observer”.

If the material element V is now allowed to move with a velocity u in the internal observer frame, the corresponding “plastic spin” W^P should be included for the co-rotational rates defined in Eq. (5) - (7). The total dislocation-induced inelastic spin, W^D associated exclusively with dislocation motion is then given by

$$W^D = \varpi^I + W^P \tag{9}$$

2.2. Observable deformation variables

The tensor β is a local variable defined at each material point and thus cannot be measured in principle by an external observer. It is then essential to introduce deformation variables that must be phenomenologically measurable and yet based on which various changes of mechanical behavior can be adequately characterized. A volume average of β as an "internal strain tensor" a, is thus defined:

$$a = \langle \beta \rangle = \frac{1}{V} \int \beta dV \tag{10}$$

where V is an appropriate material volume that must be selected to provide a meaningful measure of the respective local variables. Taking the volume average of each term in Eq. (8) provides the following kinematic relation

$$\dot{a} + \frac{\dot{V}}{V} a + \dot{\alpha} = \dot{\varepsilon} \tag{11}$$

with the two observable variables $\dot{\alpha}$ and $\dot{\varepsilon}$ defined as

$$\dot{\alpha} = \langle \nabla \cdot (v\beta) \rangle = \frac{1}{V} \int_S \beta (v \cdot n) dA \tag{12}$$

and

$$\dot{\varepsilon} = \frac{V}{\lambda} \beta = \frac{1}{V} \int_V \rho b v M dV \tag{13}$$

The unit vector n in Eq. (12) denotes the normal direction to the material boundary S. The sink source term (χβ) is neglected in Eq. (13) by assuming the usual Frank-Read source of glide dislocations [24] located at the center of slip zones.

The tensor variable $\dot{a}$ defined as the volume average of the symmetric part of the internal distortion in Eq. (10) provides an effective measure of the internal distortion due to

the stored dislocations within the time. The rate variable involving the surface integral in Eq. (12) is referred to as the "plastic strain rate tensor" since it is caused by the outward flux of dislocations across the material boundary S representing the irreversible and non-recoverable rate process of relieving the internal strain". This brings up the possibility of utilizing such an internal variables description to unify various "externally observable physical phenomena" such as plasticity, creep, crack propagation and phase transformations among others. The remaining integral defined in Eq. (13) is referred to as the "inelastic strain rate tensor" representing the total rate of inelastic deformation, similar to that of Orowan's relation for the mobile dislocation induced strain rate.

2.3. Constitutive relations

It can be easily seen from Eq. (10), (11) and (13) that a mechanic description of a, $\dot{a}$ and $\dot{\varepsilon}$ can be accomplished when the relationships of density ρ and flux j =ρν to appropriate loading parameters are known. For this purpose, a double-ended pile-up model of straight edge dislocations is considered. For this simple model, Eq. (10) now takes the form of

$$a = b\eta l^2 M \int_{-1}^{1} y\rho(y)dy = 2aM \tag{14}$$

With y= (λ/l) and η denoting the slip zone density. The density function ρ(y) must be determined by including the effect of dislocation generation and flux across the barriers. ρ(y) in a general form of $\rho(y) = \sigma^I Ø(y)/Gb$ is prescribed with G denoting shear modulus and σ^I a stress invariant quantity defined by $\sigma^I = \sigma^I M$ responsible for driving dislocations against the long-range interaction forces due to the pile-up dislocations. The remaining part of stress $\sigma^F = 2\sigma^F M$ is used for driving dislocations against the lattice friction force so that

the applied stress may be decomposed into an internal stress σ^I and a friction stress σ^F as follows;

$$\sigma = \sigma^I + \sigma^F \tag{15}$$

In view of the above relationship, the following three dimensional constitutive equation, similar to that of Hart [25], are easily arrived at;

$$a = S : \sigma^I \tag{16}$$

with the extra dividend that the fourth-order tensor S is now explicitly given by the relationship,

$$S = \frac{\eta l^2}{G} \int_{-l}^{l} y\Phi(y) dyMM \tag{17}$$

A similar expression can be found for the plastic strain rate tensor. In fact, for a double-ended pile up with the length 2*l*, Eq. (12) reduces to

$$\dot{\alpha} = 2b\eta l j^B M = 2\dot{\alpha} M \tag{18}$$

with j^B denoting the dislocation flux at the barrier. It then follows that

$$\dot{\alpha} = \frac{\dot{\alpha}}{2\sigma^I}\sigma^I = \frac{\dot{\alpha}}{a} S : \sigma^I \tag{19}$$

providing again a three-dimensional constitutive relationship for α. To proceed further an expression for j^B is needed which should depend on the temperature, barrier structure, the mechanical driving force, f^B, and resistance forces, f*, respectively. In view of the physical conditions that $j^B = 0$ for $f^B = 0$ and $j^B \to \infty$ as $f^B \to f^*$ for an activation type of kinetics process, the following is proposed:

$$\left(f^B / f^* \right) = \exp\left[-\left(j_0^B / j^B \right)^p \right] \tag{20}$$

where j_0^B is a reference flux when (f* / f^B) = *e* and the exponent *p* characterizes dislocation permeability through barriers and thus depends on the barrier properties including its geometry. For the case of plastic distortion, the Peach-Koehler type forces may be used to replace (f^B/ f*) by (σ^I/σ^*) and the flux term (j_0^B / j^B) also can be replaced by (α^*/α) to yield

$$\left(\sigma^* / \sigma^I\right) = \exp\left(\dot{\alpha}^* / \dot{\alpha}\right)^p \tag{21}$$

Eq. (21) is identical to the "plastic equation of state" proposed by Hart [25] except that the permeability parameter, p, replaces the phenomenological parameter, λ. To account for the temperature effect, it is noted that the reference rate $\dot{\alpha}^*$ is related to j_0^B prescribe the following relationship also similar to that of Hart;

$$\dot{\alpha}^* = \nu^I \left(\sigma^* / G\right)^{n^I} = \exp\left(-Q^I / RT\right) \tag{22}$$

with ν^I and Q^I denoting the jump frequency and the activation energy of leading dislocation at the barrier. In Eq. (22), R is the gas constant and n^I is a material constant.

Finally, the total inelastic strain rate given in Eq. (13) can now be expressed as

$$\dot{\varepsilon} = b\eta l \int_{-1}^{1} j(y) dy MM \cong b\eta l j^L M = 2\dot{\varepsilon} M \tag{23}$$

with j^L now denoting an average value of dislocation flux within a slip zone. Since the dislocation glide within a slip zone is governed by the lattice friction force related to σ^F, Eq. (23) can be written in a tensorial form;

$$\dot{\varepsilon} = \frac{\dot{\varepsilon}}{\sigma^F} \sigma^F \tag{24}$$

The flux j^L should, in general, depend on the temperature, lattice structure and the

driving force ($f_L - f_0$) . This flux must satisfy the physical conditions signifying a viscous drag process with $j^L = 0$ for $f_L \leq f_0$ and $j^L \rightarrow \infty$ as ($f_L - f_0$) $\rightarrow \infty$* where f_L is the force required for dislocations to overcome the short-range resistance forces including the threshold friction force f_0. The following power law relationship can then be proposed;

$$\left(j^L / j_0\right) = \left[\left(f_L / f_0\right) / f_0\right]^{1/M} \tag{25}$$

where M is constant and j_0 is a reference flux when $f_L = 2f_0$.

Replacing the flux ratio by the strain rate ratio ($\dot{\varepsilon} / \dot{\varepsilon}_0$), from the relationship given in Eq. (23), Eq. (24) reduces to the usual power law relationship between $\dot{\varepsilon}$ and σ^F;

$$\left(\dot{\varepsilon} / \dot{\varepsilon}_0\right) = \left[\left(\sigma^F - \Sigma_0\right)\Sigma_0\right]^{1/M} \tag{26}$$

with Σ_o denoting a static lattice friction stress. The temperature effect can be accounted for through j_0 which is in turn related to $\dot{\varepsilon}_0$,

$$\dot{\varepsilon}_0 = \nu^F \left(\Sigma_0 / G\right)^{n^F} \exp\left(-Q^F / RT\right) \tag{27}$$

with ν^F and Q^F denoting the jump frequency and the activation energy of glide dislocation to overcome the lattice friction.

2.4. Constitutive relationship for superplasticity

Generally, an internal stress σ^I responsible for driving dislocations against the long-range interaction forces due to the pile-up dislocations and lattice friction force σ^F used for driving dislocations against friction glide resistance between dislocation and lattice as follows;

$$\sigma = \sigma^I + \sigma^F \tag{28}$$

The constitutive relation for plastic strain rate $\dot{a}$ can be formulated as a kinetic equation of the mechanical activation process of leading-dislocation by internal stress. For uniaxial tension, the scalar relation is expressed in a similar form to that of Hart as

$$\left(\sigma_\alpha{}^* / \sigma^I\right) = \exp\left(\dot{\alpha}^* / \dot{\alpha}\right)^p \tag{29}$$

and

$$\dot{\alpha}^* = \nu^I \left(\sigma_\alpha{}^* / G\right)^{n^I} \exp\left(-Q_\alpha{}^I / RT\right) \tag{30}$$

Since a grain boundary is an atomic-level interface with low cohesive force and high diffusivity compared to a grain matrix, GBS can be regarded as a stress-induced viscous flow under a frictional drag and we have the following scalar relation between the applied stress and GBS rate;

$$\left(\dot{g} / \dot{g}_0\right) = \left[\left(\sigma - \Sigma_g\right)\Sigma_g\right]^{1/M_g} \tag{31}$$

And

$$\dot{g}_0 = \nu^g \left(\Sigma_g / \mu^g\right)^{n^g} \exp\left(-Q^g / RT\right) \tag{32}$$

As like plastic strain rate $\dot{\alpha}$, Dislocation creep strain rate $\dot{\beta}$ can be formulated also as a kinetic equation of the mechanical activation process of leading-dislocation by internal stress.

$$\left(\sigma_\beta{}^* / \sigma^I\right) = \exp\left(\dot{\beta}^* / \dot{\beta}\right)^p \tag{33}$$

and

$$\dot{\beta}^{*} = \nu^{I}\left(\sigma_{\beta}{}^{*}/G\right)^{n^{I}} \exp\left(-Q_{\beta}{}^{I}/RT\right) \tag{34}$$

With this additional strain rates, the total inelastic strain rate $\dot{\varepsilon}_T$ must now be written by adding $\dot{g}$ and $\dot{\beta}$ to Eq. (11) as

$$\dot{\varepsilon}_T = \dot{a} + \dot{\alpha} + \dot{\beta} + \dot{g} \tag{35}$$

neglecting the volume change rate neglecting the volume change rate V. From this kinematic relationship together with the stress relationship given by equation (15), a rheological model for high temperature deformation can naturally be constructed as shown in Fig. 3 together with a physical model [26]. In this model, GMD means the grain matrix plastic deformation accommodating incompatibilities due to stress-induced viscous drag.

At high homologous temperature of T>0.5Tm the friction stress σ^{F} is very small compared to the internal stress σ^{I} to give $\sigma \quad \sigma^{I}$, where Tm is the melting temperature of material in Kelvin. If tests were performed after the flow stress reached a nearly steady state to ensure that $\dot{a}$ = 0 to reduce Equation (35) into

$$\dot{\varepsilon}_T = \dot{\alpha} + \dot{\beta} + \dot{g} \tag{36}$$

Under this simplified experimental condition, it is sufficient to know the constitutive relationships of the $\dot{a}$, $\dot{g}$, and $\dot{\beta}$ elements prescribed by Eq. (29), (31) and (33), respectively.

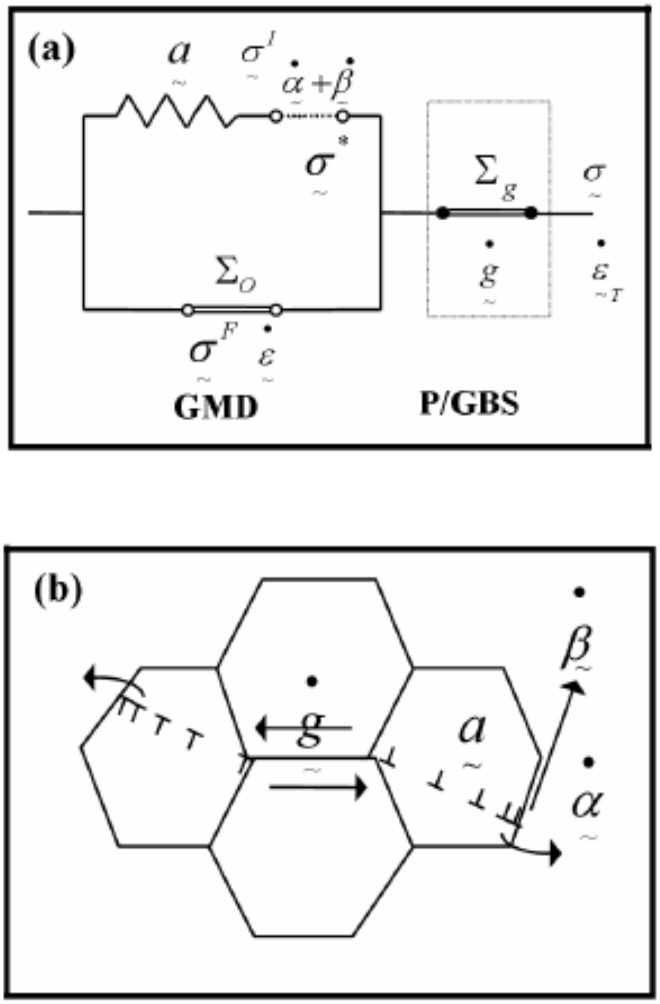

Figure 3. A physical inelastic deformation model for high-temperature deformation: (a) rheological and (b) topological model.

3. Materials and experimental procedures

The Ti-6Al-2Sn-4Zr-2Mo-0.1Si alloy used in this study was supplied by RMI in the form of a disk (i.e., sliced billet; ϕ = 155 mm × H = 18 mm) with a chemical composition (in weigh percent) of 5.55 aluminum, 1.86 tin, 4.03 zirconium, 1.90 molybdenum, 0.08 silicon, 0.06 iron, 0.13 oxygen, 0.01 carbon, 0.008 nitrogen, and balanced titanium. The microstructure of as-received material revealed relatively coarse equiaxed-alpha grain size of ~13 μm (Fig. 4a). To reduce the alpha grain size through dynamic globularization, a part of specimen machined to have a dimension of W = 100 mm × L = 80 mm × H = 18 mm was beta-solution treated at 1050 ^{o}C (beta-transus temperature at which alpha + beta $\rightarrow$ beta: ~1005 ^{o}C) for 1 h, and then, immediately quenched in water to obtain martensite microstructure with approximately 0.2-μm-thick laths (Fig. 4b). Finally, the material was cross-rolled at a temperature of approximately 775 ^{o}C using 10 % reduction per pass up to a total reduction of 80 % and quenched in water. (More details on dynamic globularization were studied in Ref. [9, 27-31]) By this means, UFG Ti-6Al-2Sn-4Zr-2Mo-0.1Si alloy was produced. EBSD map for alpha phase with tolerance angle of 15^{o} revealed alpha particle size of ~2.2 μm (Fig. 4c). In two phase titanium alloys, these high angle alpha particles are important in measuring the activation energy [16].

The low-temperature deformation behavior of CG and UFG materials was quantified *via* uniaxial-tension and load-relaxation tests. Tension specimens with a gauge length of 5 mm were machined parallel to the final rolling direction of the plate. To prevent the oxidation of surface (alpha case), which deteriorates superplasticity [32], the specimens were coated with delta glaze. All the samples were tested using INSTRON 1361 at the temperature range of 650-750 ^{o}C and the strain-rate range of 10^{-4}-10^{-2} s^{-1}. Load-relaxation tests were performed using specimens with a gauge length of 25 mm at 650-750 ^{o}C.

To compare dynamic and static coarsening behaviors of the present material, static heat treatments were also conducted at 750 ^{o}C for 24hrs and 70hrs with subsequent

quenching.

Microstructures were examined *via* OM, TEM, and EBSD analysis. For optical microscopy, Kroll's reagent (5 pct HNO_3, 10 pct HF and 85 pct H_2O) was used to etch samples. Thin foils for TEM were prepared by twin-jet electro-polishing at -40 ^oC using a mixture of 5 pct H_2SO_4 and 95 pct CH_3OH. TEM micrographs were obtained by utilizing a Cs corrected HR-STEM, JF-2200 (JEOL) operating at an accelerating voltage of 200 kV. To measure alpha grain/particle size, not sub-grain size with low-misorientation angle, unique-grain color map for alpha phase was constructed using TSL software with the tolerance angle of 15^o. For this purpose, the samples were electro-polished using LectroPol-5 (STRUERS) at a voltage of 22V for 25 seconds in a solution of 410 ml methanol, 245 ml 2-butoxy ethanol and 40 ml $HClO_4$ (60 %). Then EBSD technique was applied utilizing a Helios nanolab^{TM} 600.

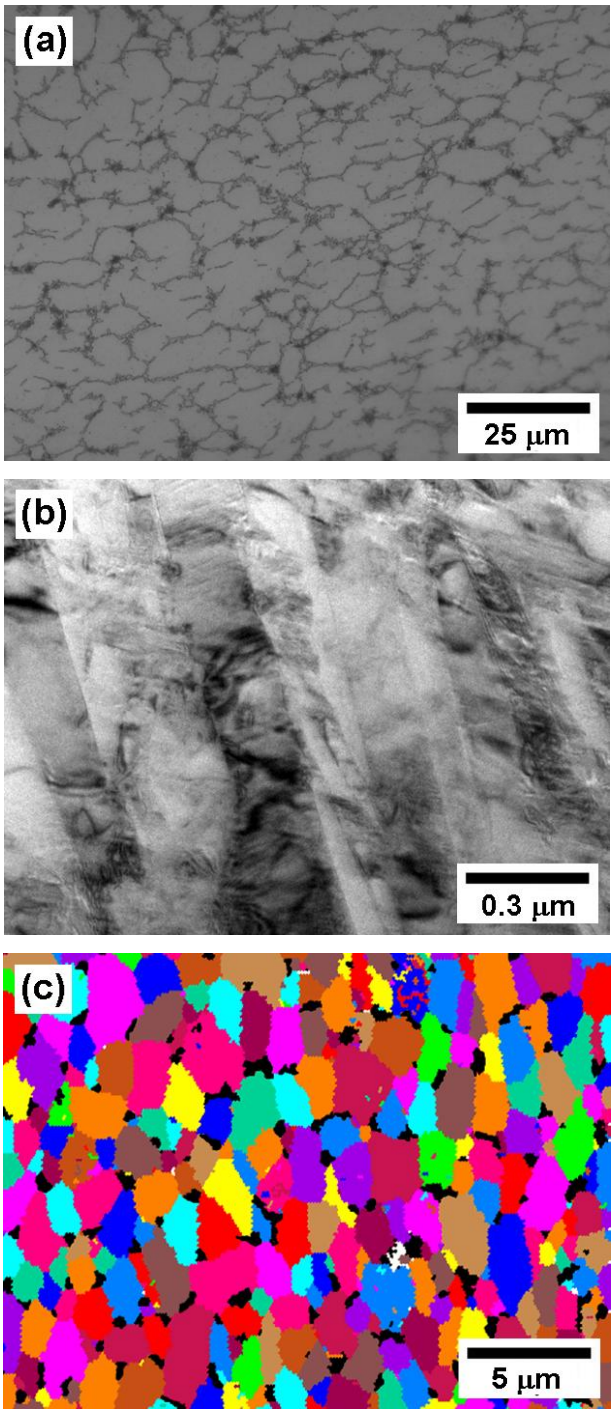

Figure 4. The micrographs showing (a) as-received microstructure (OM), (b) martensite microstructure after beta-solution treatment (TEM), and (c) dynamically globularized microstructure (unique-grain color map for alpha phase with tolerance angle of 15^{o}).

4. Results

4.1. Flow behavior and elongation to failure

Fig. 5a and b represent typical true stress *vs* true strain curves for CG and UFG Ti-6Al-2Sn-4Zr-2Mo-0.1Si alloys with the variation of strain rate at 750 ^{o}C. The overall shapes of the flow curves were similar to those reported earlier for Ti-6Al-4V alloy at temperature range of 600-725 ^{o}C, which revealed steep flow hardening and gradual decrease in flow stress with increasing strain [13,33]. Also, it was apparent that the peak stress of CG specimen was higher than that of UFG specimen at the same test condition, and the flow stresses of both materials noticeably decreased with decreasing the strain rate from 10^{-2} to 10^{-4} s^{-1}. More importantly, while the flow stress of CG specimen deformed at 10^{-4} s^{-1} decreased at relatively low strain of ~0.2, that of UFG specimen revealed quasi-stable flow up to the strain of ~2.0 resulting large elongation.

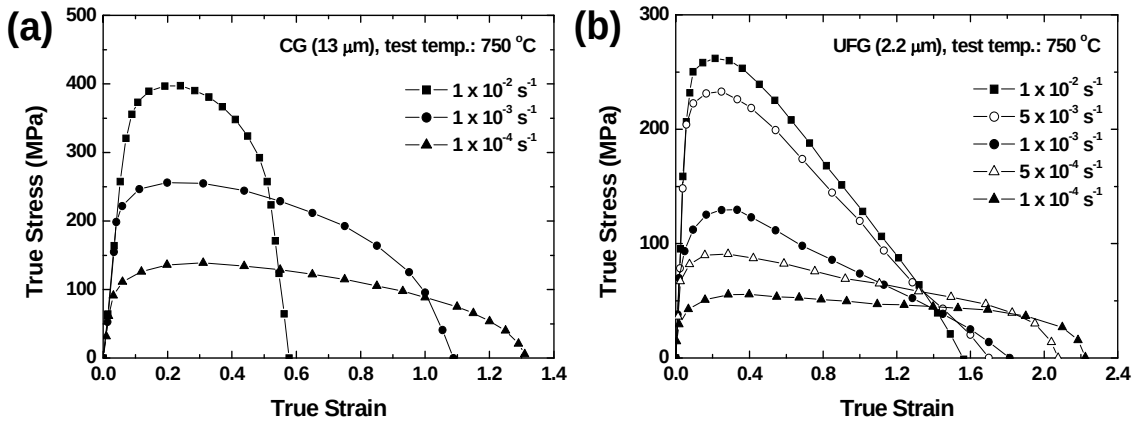

Figure 5. Typical true stress *vs* true strain curves of (a) CG (~13 μm) and (b) UFG (~2.2 μm) Ti-6Al-2Sn-4Zr-2Mo-0.1Si specimens with the variation of strain rate at 750 ^{o}C.

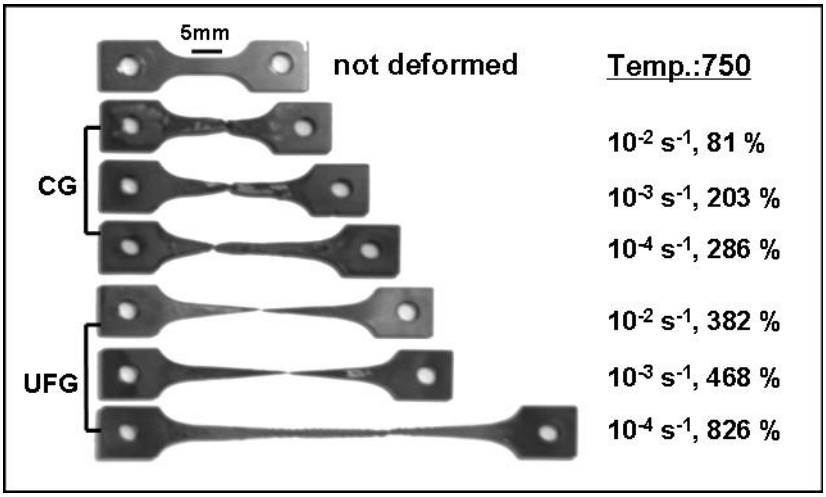

Figure 6. Macrographs of fractured tension specimens for CG and UFG materials tested at 750^{o}C with the variation of strain rate.

Elongations of specimens tested at various conditions are shown in Fig. 6. In contrast to CG materials showing moderate elongations (81-286 %), UFG specimens revealed needle-like neck, which was attributed to the extensive spreading of instantaneous necking with large elongation (382-826 %) even at 750 ^{o}C. The elongations to failure for the CG and UFG specimens were summarized in Fig. 7, combined with previously reported results obtained under conventional superplastic conditions [4]. Two aspects were noted in Fig. 7. First, the UFG material exhibited approximately 2.5 times higher total elongation as compared to the CG material at the temperature range of 650-750 ^{o}C. Second, in spite of different phase volume fraction and test temperature, the total elongations for UFG samples deformed at 750 ^{o}C were similar to those for conventional one deformed at high temperature of 940^{o}C. This large elongation of UFG Ti-6Al-2Sn-4Zr-2Mo-0.1Si specimens is attributed to the active operation of grain boundary sliding even at low temperature of 750 ^{o}C [9].

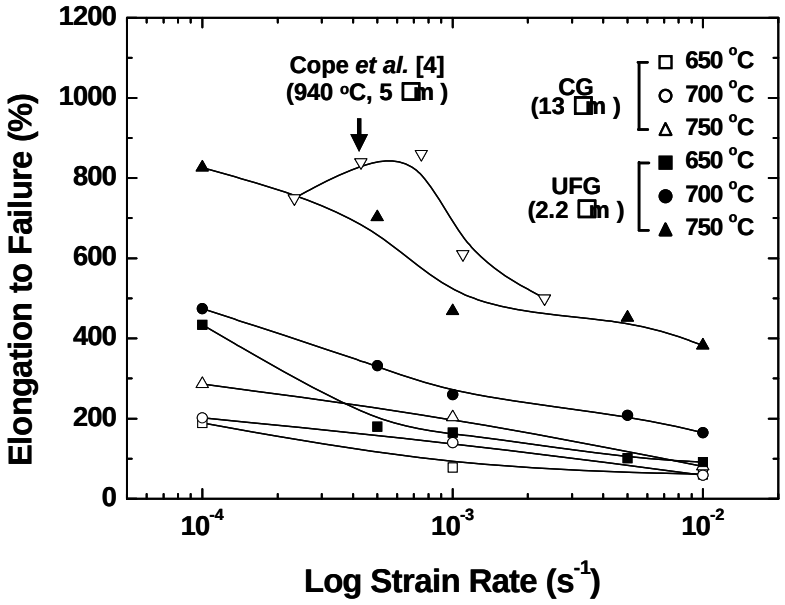

Figure 7. Elongation to failure of CG and UFG Ti-6Al-2Sn-4Zr-2Mo-0.1Si specimens tested at the temperature range of 650-750 ^{o}C.

4.2. Load-relaxation behavior

In the context of internal-variable theory, activated deformation processes such as grain-matrix deformation (GMD) and grain-boundary sliding (GBS) during low-temperature deformation can be quantitatively interpreted in for both CG and UFG Ti-6Al-2Sn-4Zr-2Mo-0.1Si alloys. For this purpose, the load-time data from load-relaxation tests were converted to stress *vs* strain-rate plots using the relations suggested by Hart [25], *i.e.*,

$$\sigma = \frac{P\left\{l_0 + \left(x - P/K\right)\right\}}{A_0 l_0} \tag{37}$$

$$\dot{\varepsilon} = -\frac{\dot{P}}{K\left\{l_0 + \left(x - P/K\right)\right\}} \tag{38}$$

where P and $\dot{P}$ is the load and its time derivation, respectively, K is the machine stiffness,

A_0 and l_0 mean the cross-sectional area and the length of the gauge section, respectively, and x is the displacement of crosshead position.

The obtained stress *vs* strain-rate curves (rectangular dot) for the CG and UFG specimens are shown in Fig. 8. With increasing temperature, the curves tended to shift toward higher strain rate and lower stress region. Although both CG and UFG specimens exhibited similar behavior, it is noted that the flow stress for UFG material decreased more steeply with decreasing strain rate as compared to that for CG specimen at the same temperature, due to its higher strain-rate sensitivity (m), which will be discussed in Section 5.2. Based on internal-variable theory of inelastic deformation, GBS, GMD and GBS+GMD were plotted as dot, dashed and solid lines, respectively, in Fig. 8. The constitutive parameters used in this study are listed in Table 1. It is apparent that the shapes of all fitted lines for the CG specimen (Fig. 8a and b) were noticeably different from those for the UFG specimen (Fig. 8c and d). The experimental data for the CG specimen was well matched with sole GMD line which was followed by Eq. (29), suggesting that the predominant deformation mechanism at 650 and 750 ^{o}C for CG samples would be GMD. However, the experimental result for UFG sample was not followed by sole GMD line revealing visible deviations, especially in the intermediate strain-rate region (10^{-5} s^{-1} $\leq$ $\dot{\varepsilon}$ $\leq$ 10^{-3} s^{-1}) (Fig. 8-(c)). In this strain-rate range, a straight line or a slight convex downward curve was observed, implying that another deformation mode as well as GMD also operated. Earlier works on other metallic systems manifested that this curvature change was mainly due to the operation of GBS [21,34]. Therefore, it was considered that GBS was dominantly operated in the UFG sample as compared to the CG specimen.

Table 1. Constitutive parameters for CG and UFG materials determined from load-relaxation tests.

		GMD parameters		GBS parameters			
Material	Temperature (^{o}C)	$Log\sigma^{*}$	$Log\dot{\alpha}^{*}$	p	$Log\sum_{g}$	$Log\dot{g}_{0}$	M_{g}
CG	650	3.01	-4.46	0.15	1.99	-7.02	0.5
(d = 13 μm)	750	2.91	-2.01	0.15	1.04	-6.30	0.5
UFG	650	3.32	-1.72	0.15	1.38	-6.25	0.5
(d = 2.2 μm)	750	3.01	-1.30	0.15	0.85	-6.21	0.5

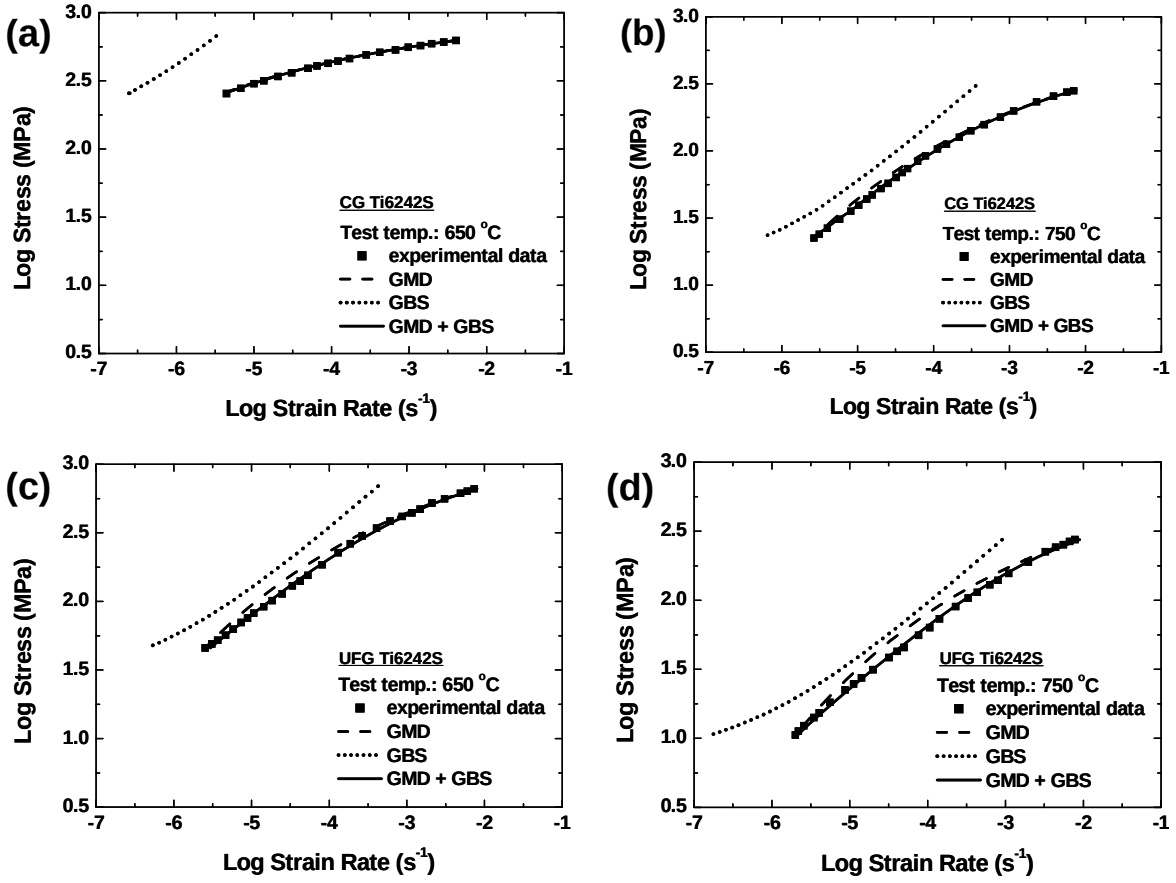

Figure 8. Comparison between experimental flow stress *vs* strain-rate data obtained by load-relaxation test (■) and predicted curves (solid lines) based on the internal-variable theory of inelastic deformation. The alpha particle sizes and test temperatures were (a) 13 μm and 650 ^{o}C, (b) 13 μm and 750 ^{o}C, (c) 2.2 μm and 650 ^{o}C, and (d) 2.2 μm and 750 ^{o}C, respectively.

5. Discussion

5.1. Dynamic and static coarsening kinetics

In view of the fact that microstructural evolution during deformation affects plastic flow behavior of the material it is worthwhile to studying coarsening kinetics of the UFG Ti-6Al-2Sn-4Zr-2Mo-0.1Si alloy. Microstructures of the tension specimens deformed at 750 ^{o}C and 10^{-4} s^{-1} are demonstrated in Fig. 9a and Fig. 9b with the variation of time, which reveal significant growth of alpha phase as compared to initial microstructure (Fig. 4c), Alpha particle size increased to 5.1 and 6.3 μm for 10hrs and 21hrs, respectively, in dynamic condition. During static annealing moderate growth of alpha phase occurred at the same temperature as shown in Fig. 9c and d; 3.1 and 4.2 μm for 24hrs and 70hrs, respectively.

Regarding the coarsening of precipitate through matrix, the diffusional analysis was developed by Lifshitz, Slyozov [35] and Wagner [36]. Recently, for the alpha/beta titanium alloy, it was elucidated by Semiatin *et al.* [14,15] that the so-called LSW theory is still valid to examine the growth of the alpha phase, although it has finite volume fraction at elevated temperature. The LSW theory is expressed in terms of the following relation.

$$\overline{r}_{\alpha}^{n} - \overline{r}_{\alpha 0}^{n} = K(t - t_0) \tag{39}$$

in which $\overline{r}_{\alpha}$ and $\overline{r}_{\alpha 0}$ denote the average alpha-particle radius at specific time (t) and initial time (t_0), respectively, K means the rate constant related to thermodynamic variables and n is the coarsening exponent indicating relevant mechanism.

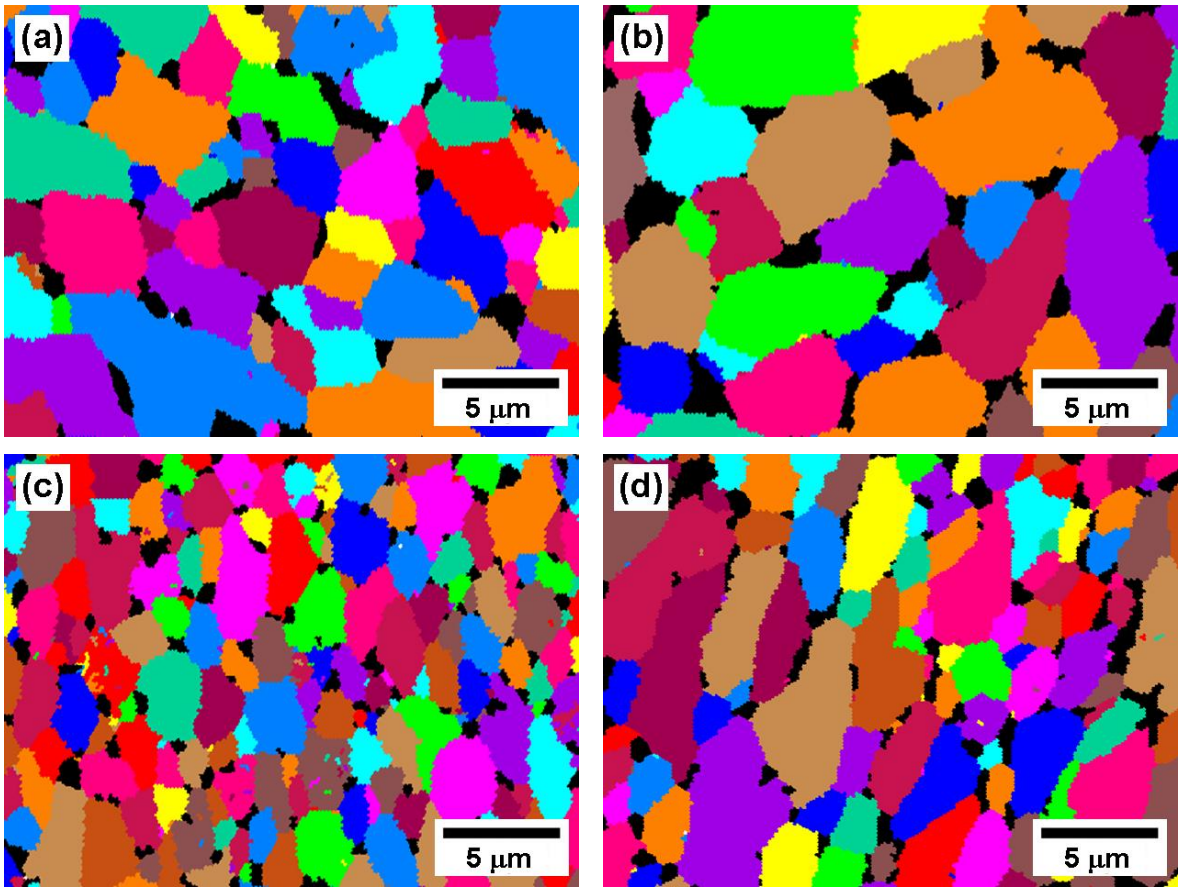

Figure 9. The unique-grain color maps (tolerance angle = 15^{o}) of the UFG specimens deformed at 750 ^{o}C and 10^{-4} s^{-1} for (a) 10hrs and (b) 21hrs. In contrast, two maps at the bottom represent microstructures static annealed at 750 ^{o}C for (c) 24hrs and (d) 70hrs, respectively.

Fig. 10a, b, and c show the experimental data fitted different *n* values (*n* = 2, 3, and 4). The best fit corresponded to *n* = 3 for both dynamic and static conditions. Thus, it is suggested that the coarsening of alpha phase for Ti-6Al-2Sn-4Zr-2Mo-0.1Si alloy is controlled by lattice diffusion through the beta matrix [37]. Growth kinetics controlled by lattice diffusion was also observed in Ti-6Al-4V alloy with ultrafine microstructure [14-16], which was consistent with our results. The value of *K* (the slope of $\bar{r}_{\alpha}^{3} - \bar{r}_{\alpha 0}^{3}$ *vs* $t - t_0$ plot in Fig. 10) is summarized in Table 2. It is important t note that the dynamic coarsening

rate (1.43 μm^3/h) was approximately 12 times higher than the static value (0.12 μm^3/h). According to previous observation on UFG Ti-6Al-4V alloy, this increase can be attributed to enhanced diffusion associated with the generation of dislocation substructure during deformation [15].

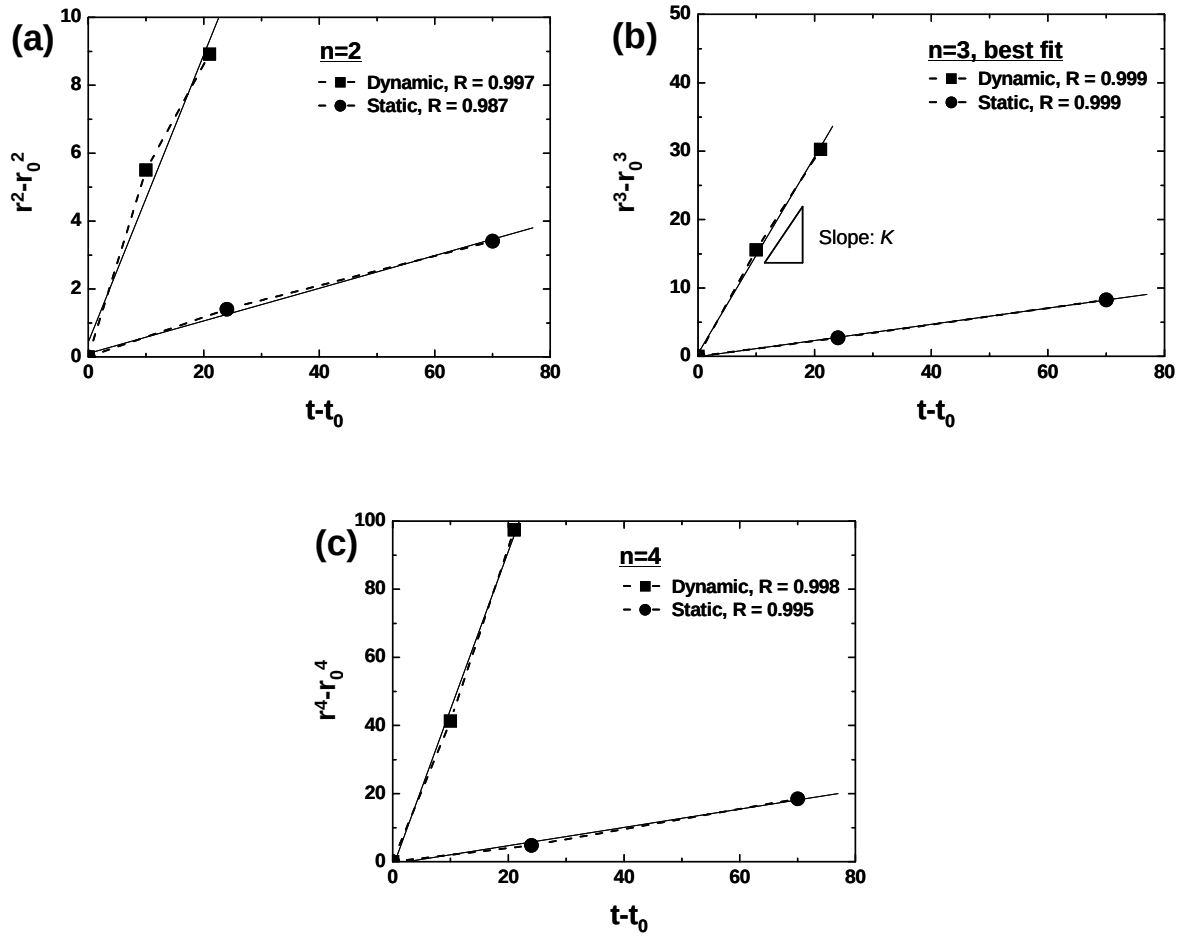

Figure 10. Plots of $\bar{r}_\alpha^n - \bar{r}_{\alpha 0}^n$ *vs* $t - t_0$ for the UFG specimen in dynamic ($\dot{\varepsilon}$=10^{-4} s^{-1}) and static conditions at 750 ^{o}C. The values of *n* correspond to (a) 2, (b) 3, and (c) 4, respectively.

Table 2. The values of rate constant K ($\mu m^3/h$) for alpha particles of Ti-6Al-2Sn-4Zr-2Mo-0.1Si and Ti-6Al-4V alloys.

Material	Temp. (^oC)	Static K ($\mu m^3/h$)	Dynamic K ($\mu m^3/h$)	D of rate-limiting solute ($\mu m^2/s$)
Ti6242S	750	0.12	1.43	0.72×10^{-3}, D of Mo from Eq. (9)
Ti64	775	0.48 [16]	3.25 [16]	4.5×10^{-3}, D of V from Eq. (10)

It is believed that diffusional growth of alpha phase of Ti-6Al-2Sn-4Zr-2Mo-0.1Si and Ti-6Al-4V alloys is rate-controlled by Mo and V solutes, respectively, through beta matrix [38]. Therefore, comparison of coarsening kinetics for these alloys is of great interest. As shown in Table 2, the rate constant (K) of UFG Ti-6Al-2Sn-4Zr-2Mo-0.1Si alloy is about 2 to 4 times lower as compared to the earlier work on UFG Ti-6Al-4V alloy at the similar temperature range (750-775 ^{o}C) [16]. For two phase titanium alloy, the rate constant in Eq. (39) can be described by the following relation [39,40].

$$K = \frac{8\left\{ f(\phi) D \gamma_{\alpha\beta} C_\beta \left(1 - C_\beta\right) V_M \right\}}{9\left\{ RT \left(C_\alpha - C_\beta\right)^2 \left(1 + \partial \ln r / \partial \ln C_\beta\right) \right\}} \tag{40}$$

where, $f(\phi)$ denotes the functional dependence of the rate on the volume fraction of alpha phase, D is the diffusivity in the beta matrix of the rate-limiting solute, $\gamma_{\alpha\beta}$ is the alpha-beta interface energy, C_β and C_α are the equilibrium concentrations in the beta and alpha phase, respectively, of the rate-limiting solute, V_M is the molar volume of the alpha phase, R is the universal gas constant, T is the absolute temperature and r is the activity coefficient of the rate-limiting solute in the beta matrix. According to the earlier works, the alpha volume fraction of the two alloys (Ti-6Al-4V and Ti-6Al-2Sn-4Zr-2Mo-0.1Si) is similar to each other at low temperature regime [4] and the growth of primary

alpha phase developed during fast quenching is also identical due to higher supersaturation and lower diffusivity of Ti-6Al-2Sn-4Zr-2Mo-0.1Si alloy [38], resulting that the effect of alpha volume fraction on the rate constant is insignificant. Although, the comparison of the other thermodynamic factors was not made in this study due to lack of data, it is apparent that the rate constant is clearly proportional to the diffusivity of the rate-limiting solute as indicated in Eq. (40). Also, Eq. (41) [38] and (42) [14] reveal that the diffusivity of the Mo solute in beta matrix for Ti-6Al-2Sn-4Zr-2Mo-0.1Si alloy is ~6 times slower than that of V solute for Ti-6Al-4V alloy at similar temperature as shown in Table 2. In this regard, it is thought that lower coarsening rate of Ti-6Al-2Sn-4Zr-2Mo-0.1Si as compared to Ti-6Al-4V alloy is due to, at least, slower diffusivity of rate-limiting solute.

$$D_{Mo}^{\beta}(\mu m^2/s) = 52500 \exp\{-18520/T(K)\} \tag{41}$$

$$D_{V}^{\beta}(\mu m^2/s) = 77000 \exp\{-17460/T(K)\} \tag{42}$$

5.2. Deformation mechanism of dynamically globularized Ti6242S alloy

In general, thermally activated deformation with a narrow strain-rate range such as the regime characterized solely by superplastic flow is expressed in terms of following constitutive equation [10,41,42].

$$\dot{\varepsilon} = A\frac{D_0 Gb}{kT}\left(\frac{b}{d}\right)^p \left(\frac{\sigma}{G}\right)^n \exp\left(-\frac{Q}{RT}\right) \tag{43}$$

in which, A is a constant, D_0 is the pre-exponential factor for relevant diffusion, b is the burgers vector, d is the grain size, k is the Boltzmann constant, G is the shear modulus, p is the grain size exponent, n is the stress exponent (n=1/m, m is strain rate sensitivity), and Q

is the activation energy which is dependent on the rate-controlling process. As pointed out in the recent research [16], alpha-particles with high angle boundaries should be considered rather than alpha sub-grains or beta grains to investigate the deformation mechanism (especially apparent activation energy for superplasticity) of two phase titanium alloys. In this study, the alpha-particle size with high misorientation angle ($\theta \geq 15^{o}$) prior to deformation (~2.2 μm) which was almost identical to the initial alpha-particle size was considered as the effective grain size. It is not surprising to observe similar alpha-particle sizes between above two microstructures (initial and prior to deformation) when considering significantly low coarsening rate of the present alloy at low-temperature region. Eq. (39) and Table 2 reveal infinitesimal growth ($D_{\alpha} = 2\overline{r}_{\alpha} = 2\sqrt[3]{K(t-t_0) + \overline{r}^{3}_{\alpha,initial}} = 2\sqrt[3]{0.12 \times 1 + 1.1^{3}}$ ~2.26 μm) of alpha particles during static heat treatment for 1h prior to test even at 750 ^{o}C.

The *n* and *p* values in Eq. (43) provide the beneficial information to determine the main mechanism activated during deformation. For example, *n* values of 1 and 2 indicate that GBS was likely accommodated by diffusional process and dislocation motion, respectively, while *p* values of 2 and 3 correspond to GBS accommodated by dislocation motion (occasionally lattice diffusion) and boundary diffusion, respectively [43,44].

To determine the *n* value, the reciprocal of *m*, a plot of stress *vs* strain rate was made on a logarithmic scale in Fig. 11. A linear-regression method was used to draw the slopes quantifying the *m* as following:

$$m = d\log\sigma / d\log\dot{\varepsilon} \tag{44}$$

For the present UFG material, two regions with different slopes were identified;

region II (10^{-4} $s^{-1} \leq \dot{\varepsilon} \leq 2\times10^{-3}$ s^{-1}) and region III ($\dot{\varepsilon} \geq 2\times10^{-3}$ s^{-1}). Such a sigmoid shape is typical for a variety of materials that exhibit superplastic behavior. In the present work, *m* was ~0.47 in region II, while that in region III was approximately 0.22 as shown in Table 3. Considering the fact that the maximum elongation is usually found in region II, it is reasonable that the higher *m* value with larger total elongation (382-826 %) was observed at a strain rate of 10^{-4} s^{-1} as compared to that (91-434 %) at a strain rate of 10^{-2} s^{-1}. Consequently, the stress exponent, *n*, in superplastic region II was found to be ~2 with UFG material. On the other hand, additional tests were conducted on specimens with alpha-particle sizes of 3.4 and 4.7 μm (Fig. 12), which was furnace cooled after heat treating at 850 ^{o}C for 6hrs and 24hrs, respectively. It is apparent that the sigmoid shapes in Fig. 11 becomes flatter due to decreasing of the slopes (*m*) in region II with increasing grain size from 2.2 to 4.7 μm at 750 ^{o}C.

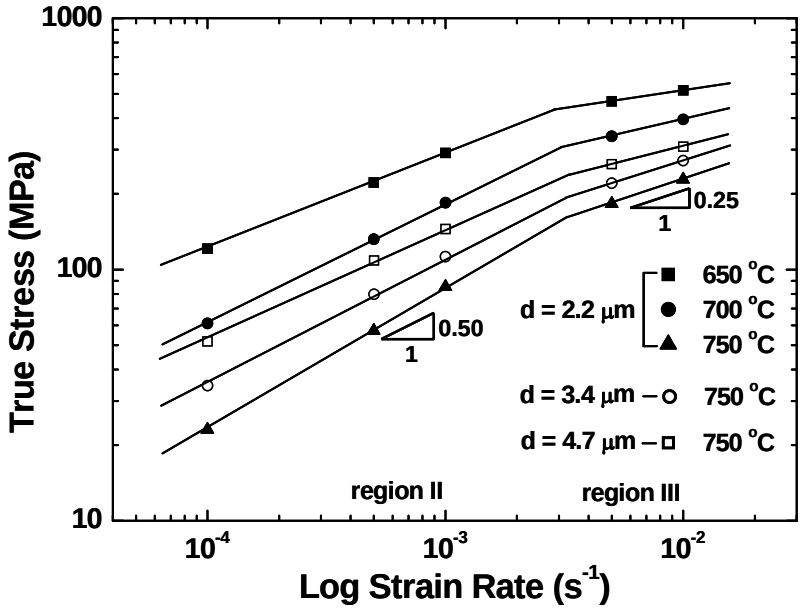

Figure 11. Logarithmic plot of true stress *vs* strain rate for the Ti-6Al-2Sn-4Zr-2Mo-0.1 alloy with variations of test temperature (650-750 ^{o}C) and grain size (2.2-4.7μm).

Table 3. The strain rate sensitivity (m) and stress exponent (n) of the UFG material at 650-750 ^{o}C.

	Strain rate sensitivity		Stress exponent	
	Region III	Region II	Region III	Region II
650 ^{o}C	0.13	0.41	7.7	2.4
700 ^{o}C	0.21	0.47	4.8	2.1
750 ^{o}C	0.31	0.53	3.2	1.9

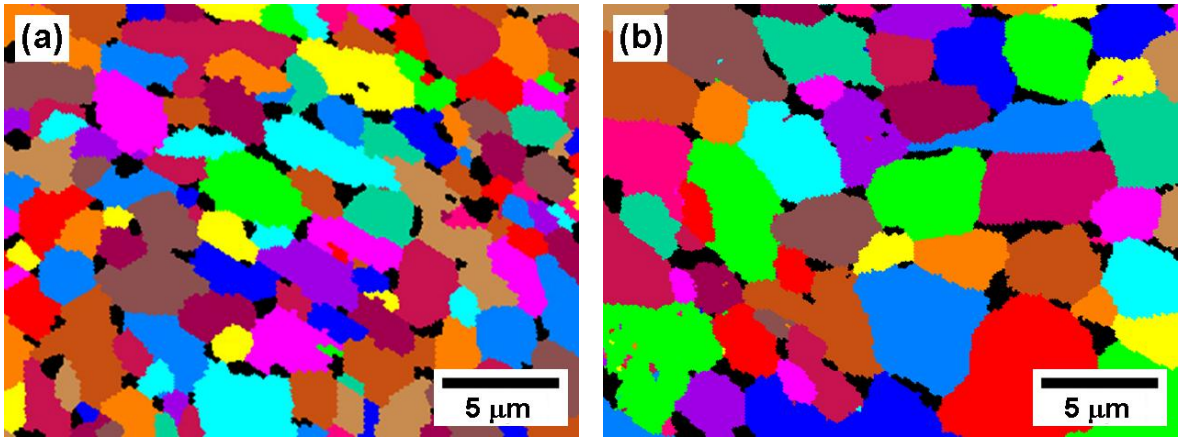

Figure 12. The unique-grain color maps with tolerance angle of 15^{o} developed in the UFG material at 850 ^{o}C for (a) 6hrs and (b) 24hrs, respectively.

In order to determine the grain-size exponent, p, the relationship between grain size and strain rate was plotted on a logarithmic scale in Fig. 13 at a fixed normalized stress (σ/G) ranging 2.0-6.5×10^{-3} where G means shear modulus at specific temperature obtained by Eq. (45) [45]. The p value (the slope in Fig 11) was measured by Eq. (46) using a linear-regression analysis. The measured grain-size exponent, p, was found to be between ~1.73 and 2.12.

$$G(MPa) = 49200 - 25.8T(K) \tag{45}$$

$$p = -\left(d\log\dot{\varepsilon}/d\log d\right)_{T,\sigma/G} \tag{46}$$

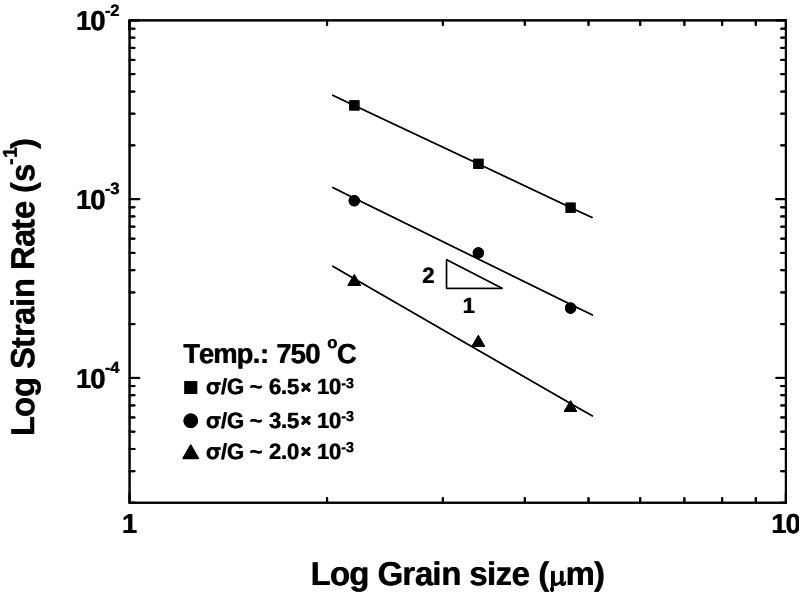

Figure 13. Logarithmic plot of grain size *vs* strain rate for the Ti-6Al-2Sn-4Zr-2Mo-0.1 alloy with the variation of normalized stress at 750 °C.

In this study, both of stress exponent (*n*) and grain-size exponent (*p*) were close to 2. Therefore, it is considered that deformation mechanism of UFG Ti-6Al-2Sn-4Zr-2Mo-0.1Si alloy in region II is GBS accommodated by dislocation motion.

It is well known that superplastic flow related to GBS accommodated by slip is rate controlled by dislocation climb rather than glide, when stress exponent, *n*, is equal to 2, due to the pile-up stress at the head of the climbing dislocation [44]. The apparent activation energy reveals information on the dominant diffusion process for climb [42,44], *e.g.*, lattice or grain boundary diffusion. From Eq. (43), the activation energy (*Q*) is derived as following:

$$Q = -R\frac{\partial \ln\left\{\dot{\varepsilon}\left(d/b\right)^{p}\right\}}{\partial\left(1/T\right)} \tag{47}$$

Fig. 14 represent the plots of not only log $\left\{\dot{\varepsilon}\left(d/b\right)^{p}\right\}$ *vs* 1/*T*, where $p = 2$ and $b =$

2.953 Å [46] at constant normalized stress (5.5×10^{-3}), but also D_{Mo}^{β} *vs* $1/T$ in which the slopes (and, hence, $Q/2.3nR$) provide the apparent activation energies for superplasticity of the UFG material and lattice diffusion of Mo solute, respectively. As shown in Fig. 14, the activation energy (Q) for the deformation of the UFG Ti-6Al-2Sn-4Zr-2Mo-0.1Si (169 kJ/mol) in region II was comparable to that for lattice diffusion of Mo (154 kJ/mol [38]), and that for lattice diffusion of Al (150 kJ/mol [47]). Furthermore, it is very close to the value for lattice diffusion of α-Ti (150 kJ/mol [48]) or β-Ti (153 kJ/mol [48]) rather than that for grain boundary diffusion of α-Ti (97 kJ/mol [48,49]) or β-Ti (137 kJ/mol [49]).

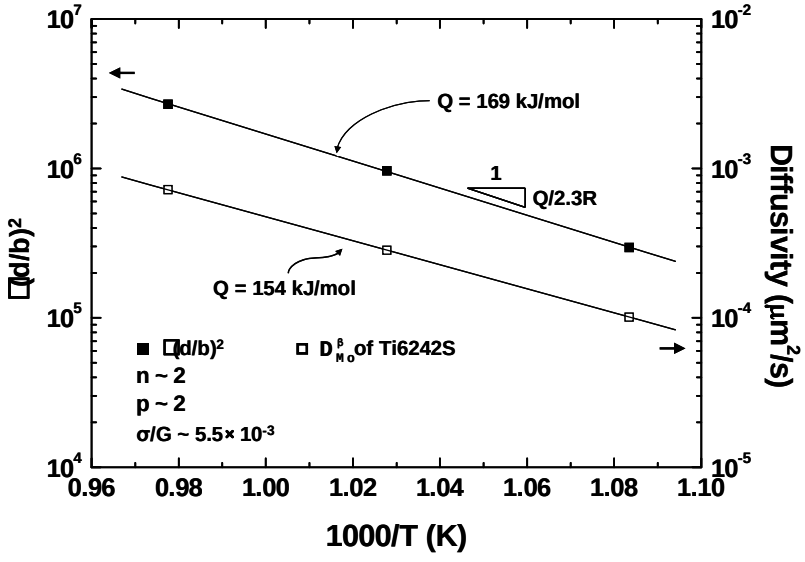

Figure 14. Comparison of activation energy for the UFG material in region II to that for diffusion of Mo solute.

5.3. Quantitative analysis on deformation mechanisms of CG and UFG materials

More detailed examination of load-relaxation behavior provides insight into the reason for enhanced superplasticity in dynamically globularized microstructure as

compared to conventional one. In the Table 1, the value of M_g were the same for both CG and UFG Ti-6Al-2Sn-4Zr-2Mo-0.1Si alloy and also identical to that for Ti-6Al-4V alloy. This is well accorded with the earlier works reporting that M_g for two phase alloy and quasi-single phase alloy is 0.5 and 1.0, respectively [13,21,50]. In addition, the strength parameter σ^* increased with decreasing grain size at the same temperature. More interestingly, it is noted that the $\sum_g$ (the friction stress for GBS) values in UFG specimens are lower than those of CG specimens at the same temperature indicating that the friction stress decreased with decreasing grain size in region II. It indicates that GBS can operate easily in the UFG microstructure. Also, the relative contribution of GMD and GBS to the whole strain is shown in Fig. 15, For both CG and UFG specimens, the GBS fraction was increased with increasing temperature from 650 ^{o}C to 750 ^{o}C. And the fraction of strain produced by GBS in UFG samples was ~35-50 %, while that of CG specimens was ~2-20 %. This well explains why very large elongation occurred in dynamically globularized material as compared to conventional one even at low-temperature region.

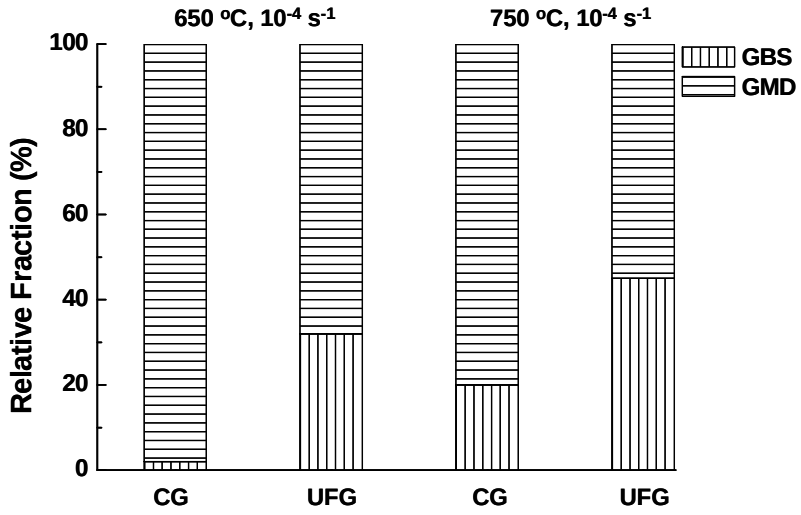

Figure 15. Relative contribution of GMD and GBS to whole deformation for the CG and UFG materials at temperatures of 650 and 750 ^{o}C and strain rate of 10^{-4} s^{-1}.

6. Summary

The low-temperature superplasticity of UFG Ti-6Al-2Sn-4Zr-2Mo-0.1Si alloy fabricated by dynamic globularization was investigated in the context of constitutive equations. The conclusions drawn in this study are as follows.

1. The unique-grain color map with tolerance angle of 15^{o} revealed that the as-received microstructure having equiaxed-alpha particle size of ~13 μm (CG) was successfully refined to ~2.2 μm (UFG) by dynamic globularization at 775 ^{o}C. The total elongations of the UFG samples (382-826 %) were considerably enhanced as compared to those of the CG specimens (189-286 %) at the same temperature ranging 650-750 ^{o}C.
2. The dynamic coarsening of alpha phase for Ti-6Al-2Sn-4Zr-2Mo-0.1Si alloy was ~12 times faster than that of static coarsening. Both static and dynamic coarsening were controlled by lattice diffusion. The coarsening rate of Ti-6Al-2Sn-4Zr-2Mo-0.1Si was much lower (2 ~ 4 times) than that of Ti-6Al-4V alloy due to lower diffusivity of rate-limiting solute at the same temperature.
3. The deformation mechanism of the low-temperature superplasticity of UFG Ti-6Al-2Sn-4Zr-2Mo-0.1Si alloy was found to be grain boundary sliding (GBS) accommodated by dislocation motion.
4. Internal-variable theory reveals that the enhancement of superplasticity in dynamically globularized microstructure was attributed to higher GBS fraction (~35-50 %) and lower friction stress ($\sum_g$) as compared to the coarse grained material.

References

[1] Boyer R, Welsch G, Collings EW. Materials properties handbook: titanium alloys. Materials Park (OH): ASM International, 1994. p.465.
[2] Williams JC, Starke EA. Acta Mater 2003;51:5775.
[3] Edington JW, Melton KN, Cutler CP. Prog Mater Sci 1976;21:61.
[4] Cope MT, Evetts DR, Ridley N. J Mater Sci 1986;21:4003.
[5] Valiev RZ, Langdon TG. Prog Mater Sci 2006;51:881.
[6] Mishra RS, Stolyarov VV, Echer C, Valiev RZ, Mukherjee AK. Mater Sci Eng A 2001:A298:44.
[7] Salishchev GA, Galeyev RM, Valiakhmetov OR, Safiullin RV, Lutfullin RY, Senkov ON, Froes FH, Kaibyshcv OA. J Mater Pro Tech 2001:116:265.
[8] Saito Y, Utsunomiya H, Tsuji N, Sakai T. Acta Mater 1999;47:579.
[9] Park CH, Ko YG, Park J-W, Lee CS. Mater Sci Eng A 2008;A496:150.
[10] Mukherjee AK, Bird JE, Dorn JE. Trans Am Soc Metals 1969;62:155.
[11] Gifkins RC. Mater Character 1994;32:59.
[12] Bae DH, Ghosh AK. Acta Mater 2000;48:1207.
[13] Ko YG, Lee CS, Shin DH, Semiatin SL. Metall Mater Trans A 2006;37A:381.
[14] Semiatin SL, Kirby BC, Salishchev GA. Metall Mater Trans A 2004;35A:2809.
[15] Semiatin SL, Corbett MW, Fagin PN, Salishchev GA, Lee CS. Metall Mater Trans A 2006;37A:1125.
[16] Sargent GA, Zane AP, Fagin PN, Ghosh AK, Semiatin SL. Metall Mater Trans A 2008;39A:2949.
[17] Arieli A, Rosen A. Metall Trans A 1977;8A:1591.
[18] Meier ML, Lesuer DR, Mukherjee AK. Mater Sci Eng A 1991;A136:71.
[19] Wert JA, Paton NE. Metall Trans A 1983;14A:2535.
[20] Seshacharyulu T, Medeiros SC, Frazier WG, Prasad YVRK. Mater Sci Eng A 2000;A284:184.
[21] Padmanabhan KA, Davis GJ. Superplasticity. Springer Verlag. Berlin, Germany, 1980.
[22] Sherby OD, Wadsworth J. Prog. Mater .Sci., 1989; 33: 169.
[23] Chang YW, Aifantis EC. Constitutive Laws for Engineering Materials; Theory and Application, edited by Desai CS, 1987; 293.
[24] Hall D, Bacon DJ. Int. Dislocations. Pergamon Press, 1983;168.
[25] Hart EW, Engng J. Mater. Tech., 1984; 106: 322.
[26] Ha TK, Chang YW. Scripta Mater., 1996; 35: 1317.
[27] Semiatin SL, Seetharaman V, Weiss I. Mater Sci Eng 1999;A263:257.
[28] Seshacharyulu T, Medeiros SC, Frazier WG, Prasad YVRK. Mater Sci Eng A 2002;A325:112.
[29] Shell EB, Semiatin SL. Metall Mater Trans A 1999;30A:3219.
[30] Kim JH, Semiatin SL, Lee CS. Acta Mater 2003;51:5613.
[31] Park CH, Park K-T, Shin DH, Lee CS. Mater Trans 2008;49:2196.
[32] Patankar SN, Kwang YT, Jen TM. J Mater Proc Tech 2001;112:24.
[33] Sergueeva AV, Stolyarov VV, Valiev RZ, Mukherjee AK. Mater Sci Eng A 2002;A323:318.
[34] Kim JS, Chang YW, Lee CS. Metall Mater Trans A 1998;29A:217.
[35] Lifshitz IM, Slyozov VV. J Phys Chem Solids 1961;19:35.
[36] Wagner C. Z Elektrochem. 1961;65:581.

[37] Martin JW, Doherty RD, Cantor B. Stability of microstructure in metallic systems. In: Clarke DR, Suresh S. Ward FRS IM, editors. Cambridge solid state science series, Cambridge University Press (Cambridge), 1997. p.251.
[38] Semiatin SL, Lehner TM, Miller JD, Doherty RD, Furrer DU. Metall Mater Trans A 2007;38A:910.
[39] Calderon HA, Voorhees PW, Murray JL, Kostorz G. Acta Metall Mater 1994;42:991.
[40] Doherty RD. Physical Metallurgy. In: Cahn RW, Haasen P, editors. North-Holland (Amsterdam), 1996. p.1363.
[41] Mishra RS, Bieler TR, Mukherjee AK. Acta Metall Mater 1995;43:877.
[42] Watanabe H, Mukai T, Kohzu M, Tanabe S, Higashi K. Acta Mater 1999;47:3753.
[43] Mukherjee AK. Mater Sci Eng A 2002;A322:1.
[44] Sherby OD, Wadsworth. J Prog Mater Sci 1989;33:169.
[45] Oikawa H, Oomori T. Mater Sci Eng A 1988;A104:125.
[46] Viswanathan GB, Karthikeyan S, Hayes RW, Mills MJ. Acta Mater 2002;50:4965.
[47] Semiatin SL, Brown TM, Goff TA, Fagin PN, Barker DR, Turner RE, Murry JM, Miller JD, Zhang F. Metall Mater Trans A 2004;35A:3015.
[48] Frost HJ, Ashby MF. Deformation-mechanism maps. The plasticity and creep of metals and ceramics, Pergamon Press (Oxford), 1982. p.44.
[49] Guo ZX, Ridley N. Mater Sci Technol 1987;3:945.
[50] Park JE, Semiatin SL, Lee CS, Chang YW. Mater Sci Eng A 2005;A410-411:124.